



The High-energy Spectrum of the Young Planet Host V1298 Tau

Girish M. Duvvuri^{1,2,3,4} , P. Wilson Cauley³ , Fernando Cruz Aguirre^{1,3,5} , Roy Kilgard⁶, Kevin France^{1,2,3} ,Zachory K. Berta-Thompson^{1,2} , and J. Sebastian Pineda³ ¹Department of Astrophysical and Planetary Sciences, University of Colorado, Boulder, CO 80309, USA; girish.duvvuri@colorado.edu²Center for Astrophysics and Space Astronomy, University of Colorado, 593 UCB, Boulder, CO 80309, USA³Laboratory for Atmospheric and Space Physics, University of Colorado, 600 UCB, Boulder, CO 80309, USA⁴Department of Physics and Astronomy, Vanderbilt University, Nashville, TN 37235, USA⁵The University of Iowa, Department of Physics & Astronomy, Van Allen Hall, Iowa City, IA 52242, USA⁶Astronomy Department, Wesleyan University, Middletown, CT 06459, USA

Received 2023 August 29; revised 2023 September 12; accepted 2023 September 14; published 2023 October 16

Abstract

V1298 Tau is a young pre-main-sequence star hosting four known exoplanets that are prime targets for transmission spectroscopy with current-generation instruments. This work pieces together observations from the NICER X-ray telescope, the Space Telescope Imaging Spectrograph and Cosmic Origins Spectrograph instruments aboard Hubble Space Telescope, and empirically informed models to create a panchromatic spectral energy distribution for V1298 Tau spanning $1\text{--}10^5$ Å. We describe the methods and assumptions used to assemble the panchromatic spectrum and show that despite this star’s brightness, its high-energy spectrum is near the limit of present X-ray and ultraviolet observatories’ abilities to characterize. We conclude by using the V1298 Tau spectrum as a benchmark for the activity saturation stage of high-energy radiation from solar-mass stars to compare the lifetime cumulative high-energy irradiation of the V1298 Tau planets to other planets orbiting similarly massive stars.

Unified Astronomy Thesaurus concepts: Pre-main sequence stars (1290); X-ray astronomy (1810); Ultraviolet astronomy (1736); Stellar atmospheres (1584); Stellar chromospheres (230); Stellar coronae (305); Atmospheric evolution (2301); Stellar magnetic fields (1610)

Supporting material: data behind figure

1. Introduction

V1298 Tau is a pre-main-sequence star that hosts four known transiting exoplanets (David et al. 2019a, 2019b). The star is bright ($d = 108.5$ pc, $m_{\text{Gaia}} = 10.1$, Gaia Collaboration et al. 2018) and similar to the young Sun ($M_{\star} = 1.101 M_{\odot}$, $R_{\star} = 1.345 R_{\odot}$; spectral type between K0 and K1.5, 23 ± 4 Myr old; David et al. 2019a), making the V1298 Tau planets prime targets for transmission spectroscopy. Both the star and its planets will change significantly over the lifetime of the system: the star will spin down, contract, and emit less high-energy radiation while the planets will contract as they both cool and lose mass from their H/He envelopes. The majority of planetary atmospheric escape is expected to take place within the first Gyr of the system’s lifetime (King & Wheatley 2021) and studying the physics of atmospheric evolution is necessary to understand exoplanet demographics and habitability. A major open question in this area is whether formation conditions or evolutionary processes like photo-evaporative mass loss (Watson et al. 1981) and core-powered heating (Ginzburg et al. 2018) are primarily responsible for the “radius valley”: an apparent sparsity of exoplanets with radii near $1.8 R_{\oplus}$ (Fulton et al. 2017). Statistical experiments have been proposed to compare predictions from both atmospheric loss mechanisms to the observed exoplanet population, but these approaches rely on input assumptions of the initial high-energy fluxes of young stars and their subsequent evolution

(Rogers et al. 2021). Determining the high-energy irradiation and atmospheric escape of young exoplanets like those orbiting V1298 Tau is necessary to assess the accuracy and precision of those input assumptions, following through to how we understand early planet atmospheres in our solar system and beyond.

This work describes the creation of a panchromatic spectral energy distribution (SED) for V1298 Tau (wavelengths from 1 to 10^5 Å) made available as a data product for the community to use when modeling this planetary system and interpreting observations of atmospheric escape. The panchromatic SED is presented in Figure 1. Section 2 lists the X-ray and ultraviolet observations contributing to the spectrum, Section 3 describes our analysis of the star’s far-ultraviolet (FUV, 1140–1710 Å) emission lines and coronal properties, and Section 4 explains the method used to predict the unobserved extreme ultraviolet (EUV; 100–912 Å) flux and compares this work’s inferred EUV flux to similar work by Poppenhaeger et al. (2021) and Maggio et al. (2023). Section 5 concludes by using the V1298 Tau spectrum to characterize the lifetime high-energy irradiation of planets orbiting solar-mass stars.

2. Observations

From 2020 through early 2022 we obtained observations of V1298 Tau’s high-energy spectrum using the Space Telescope Imaging Spectrograph (STIS; Woodgate et al. 1998) and Cosmic Origins Spectrograph (COS; Green et al. 2012) instruments on the Hubble Space Telescope (HST) and NASA’s Neutron Star Interior Composition Explorer (NICER) mission aboard the International Space Station (Gendreau et al. 2016). The ultraviolet observations cover the wavelength range

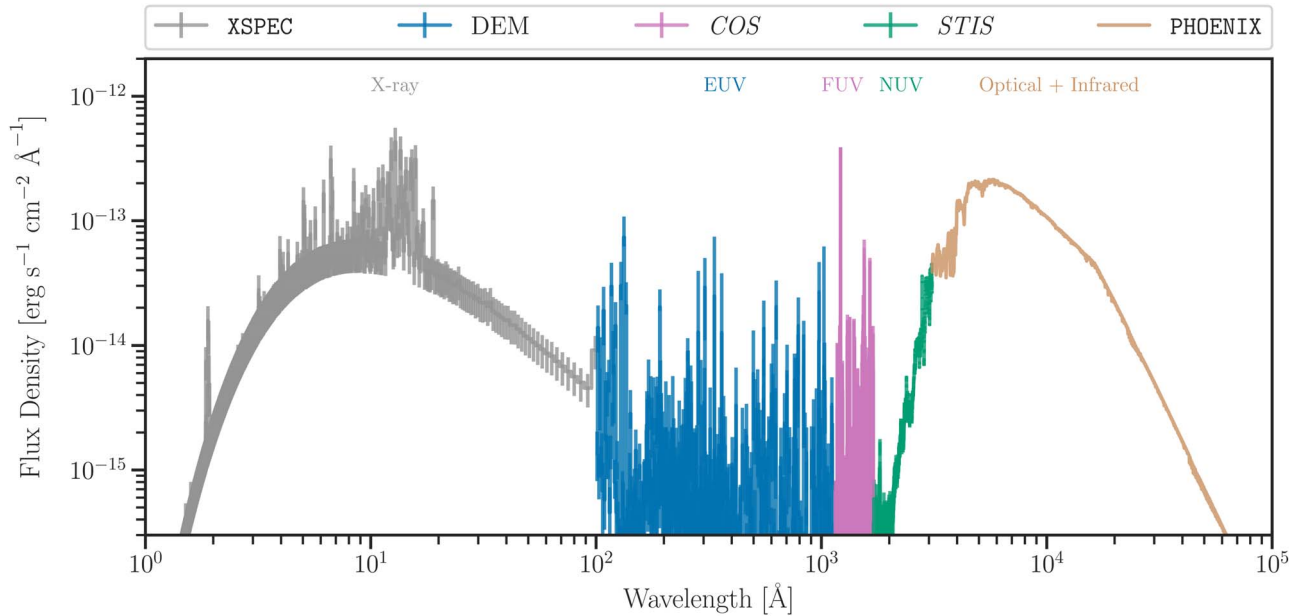


Figure 1. The composite spectrum is plotted with each component covering a specific wavelength interval at its original wavelength resolution, using data where available and supplemented by empirically constrained models. The components and their respective wavelength intervals are: XSPEC model (gray), 1–100 Å; Differential emission measure model (light blue), 100–1150 Å; HST COS data (pink), 1150–1700 Å, with two sub-intervals 1214.63–1216.78 Å ($\text{Ly}\alpha$) and 1519.42–1530.78 Å replaced with scaled excerpts from the MUSCLES SED for ϵ Eridani; HST STIS data (green), 1700–3100 Å; PHOENIX model (light brown), 3100– 10^5 Å.

(The data used to create this figure are available.)

Table 1
Summary of NICER and HST Observations

Telescope (1)	Instrument setting (2)	Date (UT) (3)	Starting Time (UT) (4)	Exposure Time (s) (5)	λ_{start} (Å) (6)	λ_{end} (Å) (7)	$\Delta\lambda^a$ (Å) (8)
NICER	...	2020-09-13	11:06	1880	5	55	0.9
NICER	...	2020-10-18	23:37	2134	5	55	0.9
HST	STIS G230L	2020-11-07	06:44	21924	1600	3150	3.0
HST	COS G160M	2020-10-17	14:54	1998	1350	1710	0.09
HST	COS G130M	2021-12-23	10:44	9892	1140	1420	0.09
		2022-01-17	03:18	12030	1140	1420	0.09

Note.

^a Resolutions vary across the free spectral range. We report the approximate value at the central wavelength of the recorded spectrum.

1140–3150 Å and the X-ray observations span the energy range 0.1–10 keV (≈ 5 –55 Å). We detail the individual instrument settings and observations in the two subsections below, including a summary in Table 1.

2.1. Hubble Space Telescope

The HST observations (GO 16163, PI–P. Cauley) were designed to span the FUV and near-ultraviolet (NUV; 1710–3150 Å) spectral ranges with minimal gaps in coverage. To accomplish this we utilized two COS settings and a single STIS setting. The COS observations were obtained with the G130M and G160M gratings and cover the FUV wavelengths and the STIS observations were performed with the G230L grating to cover the NUV spectral range. We note that the COS G130M observations were executed during transits of V1298 Tau c with the goal of measuring mass loss from the planet’s atmosphere. The transit observations will be detailed in an upcoming paper. Here, we combine the first two out of four

G130M visits into a high-quality FUV spectrum to be included in the final SED data product. The transit depth of V1298 Tau c is $<0.2\%$ (David et al. 2019a) and the presence of transits during the FUV observations has negligible impact on the total line flux measurements from the coadded spectrum.

2.2. NICER

NICER is a soft X-ray telescope whose primary purpose is to investigate the equation of state of the interiors of neutron stars. NICER was designed to have high photon arrival time accuracy and is able to record events with a precision of <300 nanoseconds, but its excellent soft X-ray sensitivity also makes it useful for observing the high-energy emission from stellar coronae. NICER only has a single configuration so we do not specify the instrument Grating/Setting in Table 1. We obtained ≈ 4 ks of exposure time through NICER’s Guest Observer Program Cycle 2 (proposal number 3041, PI–Cauley) on two

Table 2
Spectral Fits to NICER Observations

NICER ID	Temperature (keV)	Abundance	χ^2 /D. O. F.	Observed Flux (0.1–10 keV) (erg cm ⁻² s ⁻¹)
3541010201	0.79 ± 0.015	0.11 ± 0.013	293.7/96	1.84 × 10 ⁻¹²
3541010301	0.79 ± 0.014	0.14 ± 0.017	109.54/82	1.81 × 10 ⁻¹²

separate dates: 1880 s on 2020 September 13 and 2134 s on 2020 October 18.

3. Analysis

We analyzed the X-ray and FUV data to provide constraints for estimating the EUV spectrum and the intrinsic stellar Ly α profile. To complete the panchromatic spectrum beyond the HST STIS G230L observations we follow the MUSCLES approach and use a PHOENIX model with $T_{\text{eff}} = 5000$ K, $\log g = 4.0$, $[\text{Fe}/\text{H}] = 0.0$ (Husser et al. 2013), resampled to a wavelength resolution of 1.5 Å and rotationally broadened to 23 km s⁻¹. After scaling the PHOENIX model to match the STIS data at 3100 Å, the model and data showed good agreement between 2800 and 3100 Å, suggesting that this model is a good approximation for this star’s spectrum at longer wavelengths. The scaled PHOENIX spectrum component covers 3100–10⁵ Å. While there is an optical and infrared spectrum of V1298 Tau (Feinstein et al. 2021) from 4000 to 10⁴ Å, there is no overlap with the STIS data and aligning the flux calibration of this chunk of the spectrum between portions of the PHOENIX model was beyond the scope of this work.

3.1. X-Ray Analysis

We processed both NICER observations using NICERDAS 9/HEASoft 6.30 (Nasa High Energy Astrophysics Science Archive Research Center (Heasarc), 2014) to generate cleaned event lists, extract spectra, and generate observation-specific response functions. We estimated the background levels using the nibackgen350 tool of Remillard et al. (2022) and modeled the spectra in XSPEC (Arnaud 1996) with photoelectric absorption and a Raymond–Smith optically thin thermal plasma model (Raymond & Smith 1977). The spectral fit parameters and fluxes were nearly identical in both NICER observations (see Table 2), with $n(\text{H I}) = 2.42 \pm 0.54 \times 10^{20}$ cm⁻², a plasma temperature of $k_{\text{B}}T = 0.79 \pm 0.015$ keV, subsolar metallicity abundance (≈ 0.1), and an observed flux in the 0.1–10 keV band of 1.8×10^{-12} erg cm⁻² s⁻¹. A plot of the observed X-ray spectrum and model for the second observation is shown in Figure 2. For the final data product we use the XSPEC model for wavelengths below 100 Å and adopt a conservative flat uncertainty of 30% across this component of the SED.

3.2. Far-UV Emission Line Measurements of V1298 Tau

V1298 Tau was observed with the medium-resolution far-UV modes of COS (G130M and G160M; Green et al. 2012) as part of GO 16163 (PI–P. Cauley). These observations (program ID GO 16163, visits 2, 3, and 4) were acquired between 2020 October 17 and 2022 January 17. G130M observations were acquired in the CENWAVE 1291, FP-POS 4 setting, and G160M observations were acquired in the CENWAVE 1533 setting using all four FP-POS tilts. Together, these observations create a nearly continuous FUV spectrum

from 1140 to 1710 Å, with an 11 Å gap around 1525 Å where the COS detector segments are physically separated, and mitigate the effects of fixed pattern noise. The one-dimensional spectra produced by the COS calibration pipeline, CALCOS, were aligned and coadded using the custom software procedure described by France et al. (2012). The final FUV spectrum has a point-source resolution of $\Delta v \approx 20$ km s⁻¹ with 6–7 pixels per resolution element. A three-pixel boxcar smoothing was applied prior to fitting the emission lines. The total far-UV exposure times were 21,924 s in G130M and 1998 s in G160M.

The chromospheric, transition region, and coronal emission lines in the COS spectra were fitted with an interactive multi-Gaussian line-fitting code optimized for COS emission line spectra. This code assumes a Gaussian line-shape convolved with the wavelength dependent line-spread function, then uses the MPFIT routine to minimize χ^2 between the fit and data (Markwardt 2009; France et al. 2012). A second-order polynomial background, the Gaussian amplitudes, and the Gaussian full width at half maximum) for each component are free parameters. The parameters of the underlying Gaussian emission lines are returned to the user, and the total line fluxes (Table 4) are used as inputs to the DEM calculations described in Section 4.1. Figure 3 presents the spectrum and line fit for the C IV emission line as an example of the data and line-fitting procedure.

3.3. Ly α Recovery

Stellar Ly α emission is obscured by HI in the interstellar medium (ISM) which attenuates the line core. Observing Ly α with HST, whose orbit lies within the Earth’s exosphere, is further complicated by geocoronal Ly α emission, otherwise referred to as airglow. For COS data, the airglow signal cannot be separated from the stellar signal during the standard background subtraction routine. Cruz Aguirre et al. (2023; hereafter referred to as CA23) developed a tool which subtracts airglow emission from COS data to recover the underlying stellar Ly α emission by simultaneously fitting the intrinsic stellar emission, ISM absorption, and the contaminating airglow. While the tool was designed for main sequence F-, G-, K-, and M-type dwarf stars in the stellar neighborhood ($\lesssim 80$ pc), we attempted to use the tool to recover the faint Ly α emission of V1298 Tau. Due to the distance to V1298 Tau being larger than what the tool was optimized for, we increased the maximum HI column density to 10^{20} cm⁻², based on measured column densities at similar distances being $\sim 10^{19.6}$ cm⁻² (Wood et al. 2005). The spectral location of the airglow profile changes over time due to the motion of the spacecraft and the time elapsed between COS observations was large enough to require separate airglow subtractions for each individual observation.

The contaminating airglow dominates the observed spectrum, as shown in Figure 4, leaving behind little flux to inform the reconstruction of the intrinsic stellar emission line profile. The retrieval is further complicated by the effects of gain sag

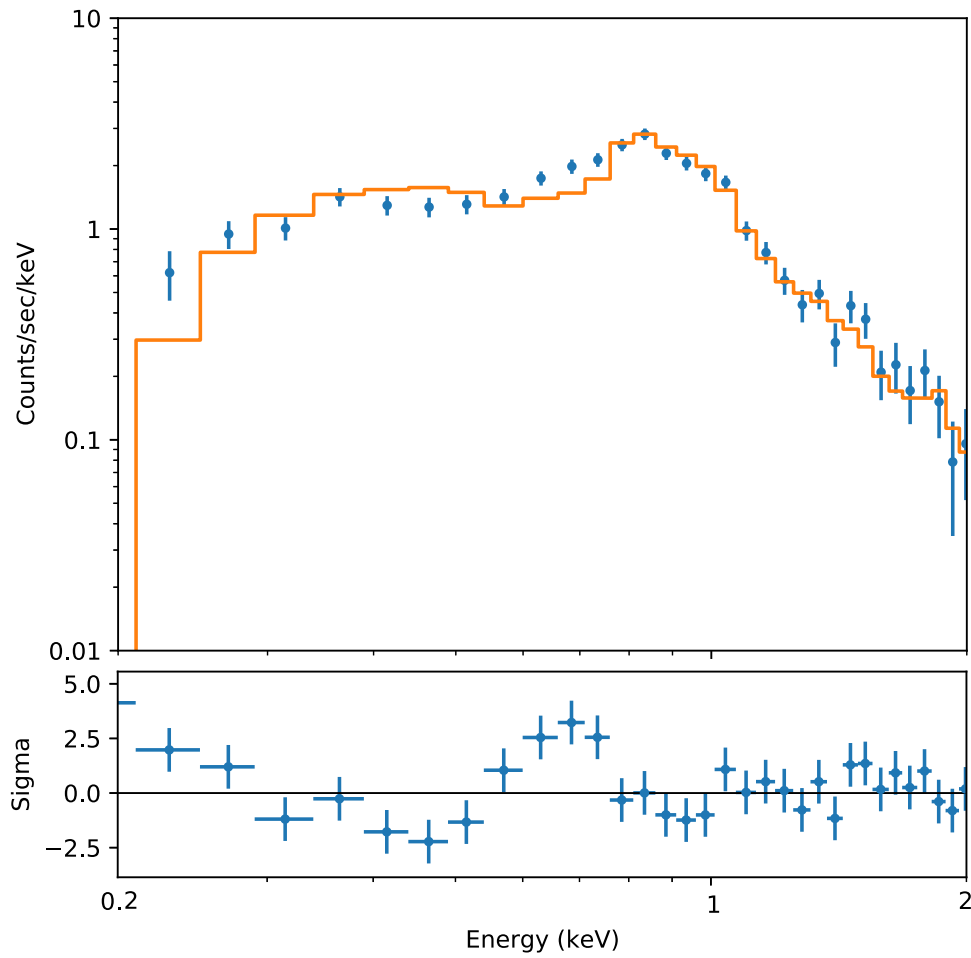


Figure 2. The NICER spectrum from the October 2020 observation is plotted as blue circles with error bars while the best-fit XSPEC model is plotted in solid orange. The model fits the continuum and strong emission lines at intermediate energies well but is less consistent with the emission from low energies.

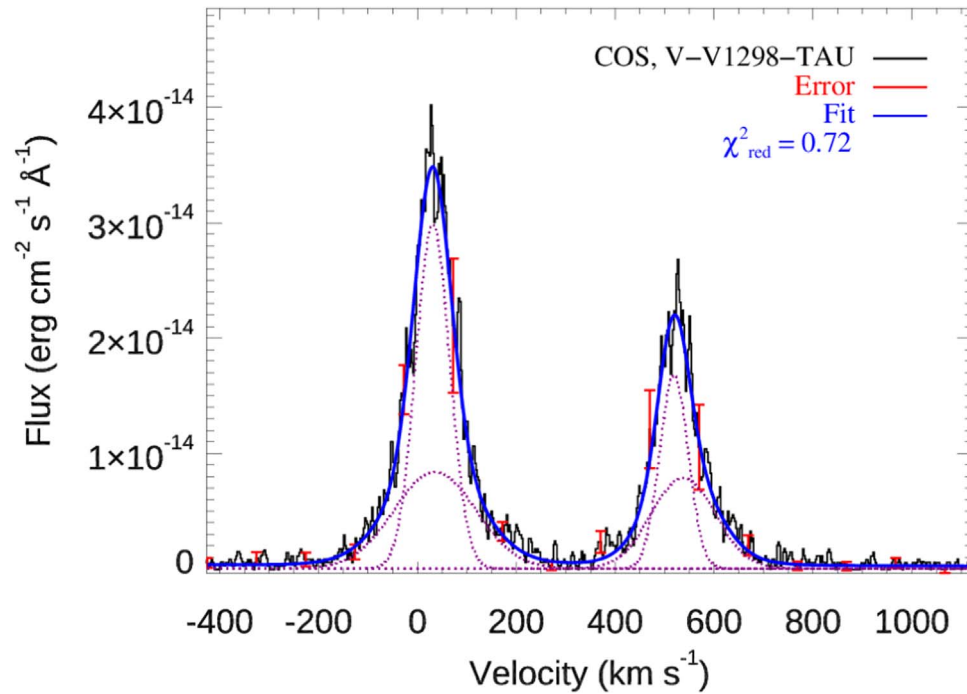


Figure 3. The C IV doublet from V1298 Tau. COS/G160M spectra are shown as the black histogram, with representative error bars in red. A two-component Gaussian fit is shown overlapped; individual components are in the dashed magenta lines and the overall fit is in solid blue.

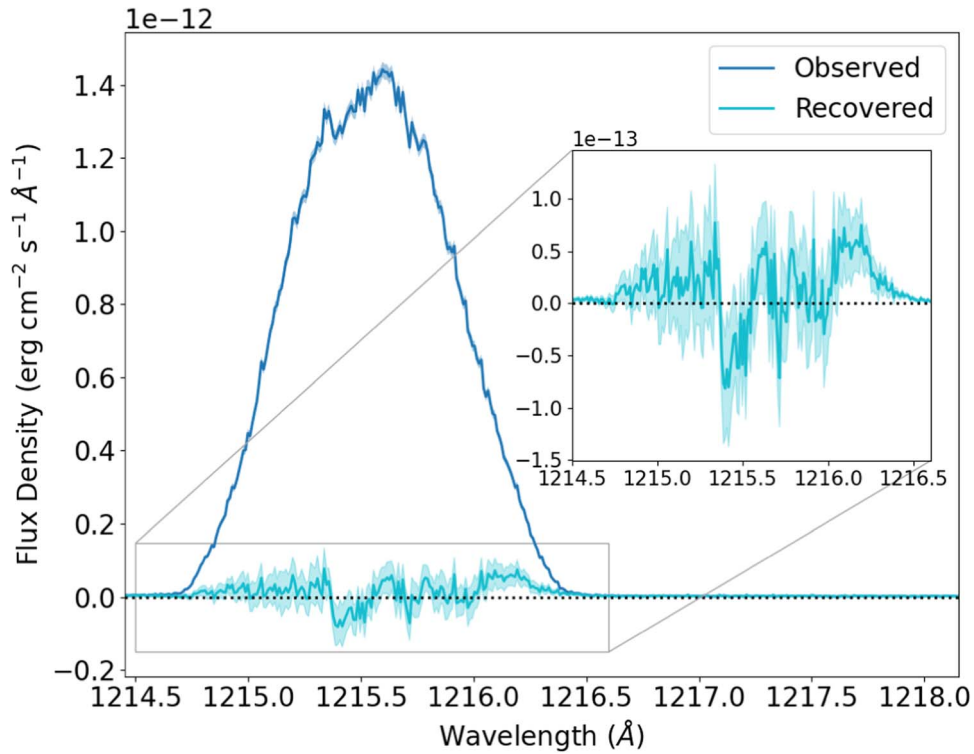


Figure 4. $\text{Ly}\alpha$ airglow subtraction of V1298 Tau. The spectrum as observed by COS is shown in dark blue. The CA23 tool is used to subtract the airglow, resulting in the recovered (ISM attenuated) spectrum in light blue. The recovered signal of V1298 Tau is faint, and a reliable reconstruction of the stellar emission was not possible.

Table 3
Ly α Predictions From Correlations

Input Variable	Input Quantity (various)	Predicted Ly α (10^{-13} erg s $^{-1}$ cm $^{-2}$)	Reference
–	–	–	–
$\log_{10} L_{\text{Si iii}}/L_{\text{bol}}$	–5.61	1.0	CA23
$\log_{10} L_{\text{N v}}/L_{\text{bol}}$	–5.87	3.0	CA23
Rossby number	assumed saturation regime $< Ro_c = 0.21$	6.8	Pineda et al. (2021)
\log_{10} Mg II hk doublet Surface Flux	6.35	1.2	Wood et al. (2005)

on the COS detector in the vicinity of geocoronal Ly α , which reduces the throughput of the stellar signal and was the primary cause for failed Ly α recoveries in CA23. Only two of the three recovered profiles were consistent in their shape, and were coadded together to try to improve the quality of the fit, but the results were poorly constrained and unstable even after multiple simplifications to the model constraining the intrinsic line profile. Therefore we elected to estimate the Ly α flux of V1298 Tau using empirically calibrated scaling relations.

There are multiple correlation methods to predict the integrated Ly α flux using other more accessible quantities, divided into either measured fluxes from emission lines or stellar parameters. These correlation methods are calibrated using samples of nearby stars where Ly α reconstructions are more viable, but these are typically main-sequence stars. Table 3 lists the Ly α flux predicted by a number of relations available in the literature, each using different activity tracers or proxies. All relations from CA23 and Wood et al. (2005) take the form of a power law, while the Pineda et al. (2021) prediction uses the saturation value of the Ly α $\frac{F_{\text{Ly}\alpha}}{L_{\text{bol}}}$ broken-power-law relation because V1298 Tau is a fast enough rotator to be in the saturated regime. We adopt the integrated flux

predicted by the Wood et al. (2005) Mg II relation because the other line-based relations are from transition region lines, formed over a narrower spatial and temperature range than Ly α .

We chose to scale the Ly α reconstruction of ϵ Eridani from the MUSCLES data products (France et al. 2016; Youngblood et al. 2016) because it is the youngest K star with a published high-quality Ly α reconstruction informed by multiple high S/N observations. We scale the MUSCLES ϵ Eridani reconstruction by the ratio between the Ly α flux predicted by the Mg II relation, 1.2×10^{-13} erg cm $^{-2}$ s $^{-1}$, and the integrated Ly α flux reported by Youngblood et al. (2016) for the ϵ Eridani reconstruction, 6.1×10^{-11} erg cm $^{-2}$ s $^{-1}$. We replace the portion of the observed COS spectrum with a scaled version of the ϵ Eridani reconstruction in the interval 1214.63–1216.78 Å, where the boundaries are identified by the intersection points between the original observed spectrum and the scaled reconstruction. We assign error bars that assume an uncertainty of a factor of 2 in either direction to be conservative. We expect that the true profile of V1298 Tau would have stronger pressure broadened wings, but most exoplanet applications of the Ly α flux for photochemistry are insensitive to the profile. If a reliable Ly α reconstruction for a closer analog to V1298 Tau

becomes available in the future, we can update the data product accordingly. We also scale the ϵ Eridani MUSCLES spectrum to fill in the FUV detector gap of the SED from 1519.42–1530.78 Å, using the flux ratio of the nearby Si IV 1394/1403 Å resonance doublet to determine the scaling factor in this spectral region.

4. Extreme Ultraviolet

The EUV spectra of most stars are poorly constrained. The only facility to observe across this wavelength regime was the Extreme Ultraviolet Explorer (EUVE) which was operational from 1992 to 2001 and was not sensitive enough to obtain high signal-to-noise spectra for most main-sequence stars unless they were highly active and nearby. This has proven to be a significant obstacle to studying stellar magnetic activity and exoplanet atmospheric escape. In the absence of data for most stars, one must either rely on other observed quantities like the X-ray or Ly α flux and then use correlations between that quantity and the EUV flux of the few stars observed by EUVE (Linsky et al. 2014; Youngblood et al. 2016; France et al. 2020), or use a model of the star’s atmospheric structure above the photosphere (Fontenla et al. 2016; Peacock et al. 2020; Tilipman et al. 2021).

4.1. Differential Emission Measure

We use the differential emission measure (DEM) technique, described in detail in Duvvuri et al. (2021) and variations of which have been used in a number of cases to estimate the XUV irradiation of exoplanets (Sanz-Forcada et al. 2004, 2011; Louden et al. 2017; Diamond-Lowe et al. 2021, 2022), to estimate the extreme ultraviolet spectrum of V1298 Tau and fill in the gaps between observations. The DEM method uses observed emission to constrain the density and temperature structure of the upper stellar atmosphere expressed as a one-dimensional function of temperature $\Psi(T) = n_e n_H \frac{ds}{dT}$ (i.e., the differential emission measure), and then combines this function with atomic data to predict unobserved emission produced from the same plasma that emitted the observed flux. The DEM function can be conceptually described as a collision or reaction rate for exciting electrons to higher states weighted by the amount of plasma along the line-of-sight at a given temperature (Craig & Brown 1976; Kashyap & Drake 1998; Duvvuri et al. 2021). The intensity of a specific emission feature can be determined by using atomic data to construct its “contribution function” (the energy contributed by this feature from an optically thin plasma at a particular temperature), weighting this function by the DEM, and then integrating over temperature. The peak of the integrand is the “formation temperature” $T_{\text{formation}}$. To constrain the DEM, it is ideal to have measurements of multiple emission features that each have very narrowly peaked contribution functions to minimize the degeneracy of DEM shapes that could produce the observed emission, and whose formation temperatures densely occupy the full temperature range of interest (10^4 – 10^8 K for the stellar upper atmosphere).

We update the method described in Duvvuri et al. (2021) by using a more recent version of CHIANTI (v10.0.1; Dere et al. 1997; Del Zanna et al. 2021) and incorporating the recombination continua of hydrogen and helium species (this updated method was also used in Feinstein et al. 2022). As described in Duvvuri et al. (2021), we use a 5th order

Chebyshev polynomial to describe the functional form of $\log_{10} \Psi(T)$, assume the method has a parameterized intrinsic uncertainty that is a temperature-independent fraction s of the predicted flux, and evaluate the likelihood of a given DEM function by directly comparing the observed line flux to the flux predicted by integrating the product of the DEM and contribution function in a Markov chain Monte Carlo (MCMC) sampler. Our approach differs from the iterative Monte Carlo method (Sanz-Forcada et al. 2004) by allowing a greater range of “acceptable” solutions; not just finding the “best” DEM for a given Monte Carlo sample of line flux distributions, but any DEM that produces a likely fit to the data. Our approach also differs from the more closely related method employed by Diamond-Lowe et al. (2021) that used Chebyshev polynomials and MCMC sampling like Duvvuri et al. (2021) but evaluated the likelihood in DEM-space, using the integral of the contribution function to determine an “average DEM” value associated with each observed emission line and fitting to these averages, a method which has significant computational advantages but again restricts the range of allowed DEM shapes by neglecting the width and shape of the contribution function. We use the `emcee` (Foreman-Mackey et al. 2013) affine-invariant implementation of the Metropolis–Hastings MCMC algorithm (Goodman & Weare 2010) to sample the joint posterior distribution of the six Chebyshev polynomial coefficients and s -factor systematic uncertainty. We ran 25 chains for $2.2 \times 10^4 \lesssim 110\tau$ steps, where $100 < \tau < 200$ steps is the range of autocorrelation times for all parameters calculated by `emcee`, and discard the first 2×10^3 steps from all walkers.

The X-ray spectral bins used to constrain the high-temperature end of the corona were selected by downsampling the spectral resolution of the XSPEC model spectrum to $R = \frac{\lambda}{\Delta\lambda} = 40$ to ensure all emission line profiles were contained within spectral bins, then identifying which bins had the highest integrals of their contribution functions. The chosen bins correspond to the strong emission lines between 0.7 and 1.1 keV shown in Figure 2, but each bin contains blends from multiple emission lines that cannot be resolved. The FUV constraints are more straightforward, the summed flux from observed emission lines of different species, with integrated fluxes from the line profile fits described in Section 3.2, where we use lines that have not been significantly impacted by interstellar reddening. V1298 Tau is active enough that we were able to observe the Fe XXI 1354 Å coronal emission line, which provides a constraint at temperatures similar to the X-ray spectral bins and these appear to agree with each other.

Figure 5 shows the distribution of DEM shapes that fit the data, with the median DEM value represented by a solid blue line and the shaded region filling in the interval between the 16th and 84th percentile boundaries of DEM values returned by the sampled polynomial shapes. The horizontal lines represent constraints imposed by the observed fluxes, with the width encompassing the central 68% of the cumulative integral of the contribution function and the y -value representing the average $\bar{\Psi}$ value obtained by dividing the flux by the integral of the contribution function (treating the DEM Ψ as locally constant). These averages are illustrative and meant to show which temperatures are constrained by which measurements, color-coded to distinguish between the FUV lines (light pink) and X-ray spectral bins (gray). Figure 6 compares the predicted

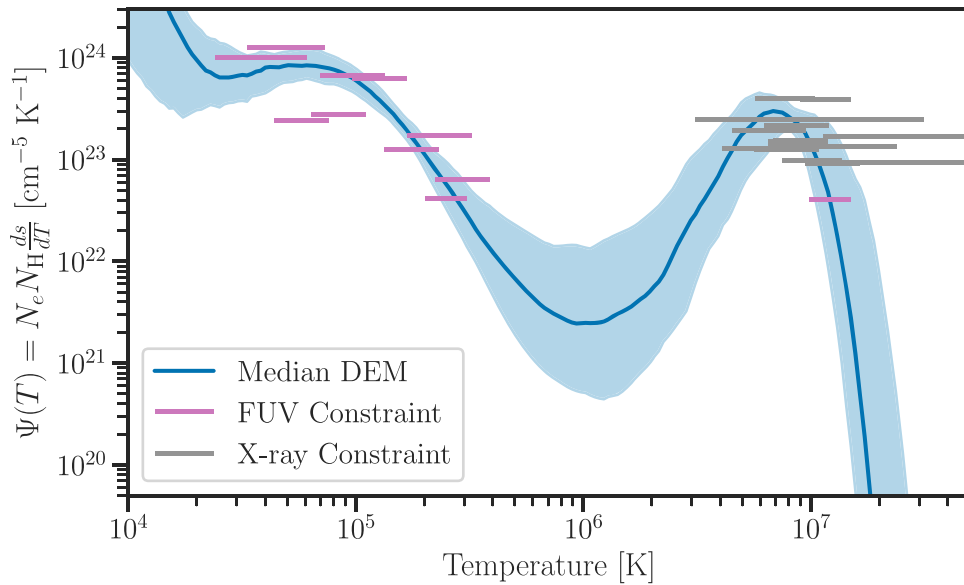


Figure 5. The differential emission measure model fit compared to representative average DEM values derived from the observed fluxes used to constrain the fit. The uncertainty of allowed DEM shapes is greatest in the interval between 3×10^5 K and 3×10^6 K where there are no observed emission features formed at specifically those temperatures. The peak at 6×10^6 K corresponds to the corona and the DEM turning down prevents the formation of emission lines at temperatures greater than 1.5×10^7 K, which is consistent with the isothermal XSPEC model fit to the X-ray data. Figure 6 compares the fluxes predicted by the DEM model to the observed flux constraints.

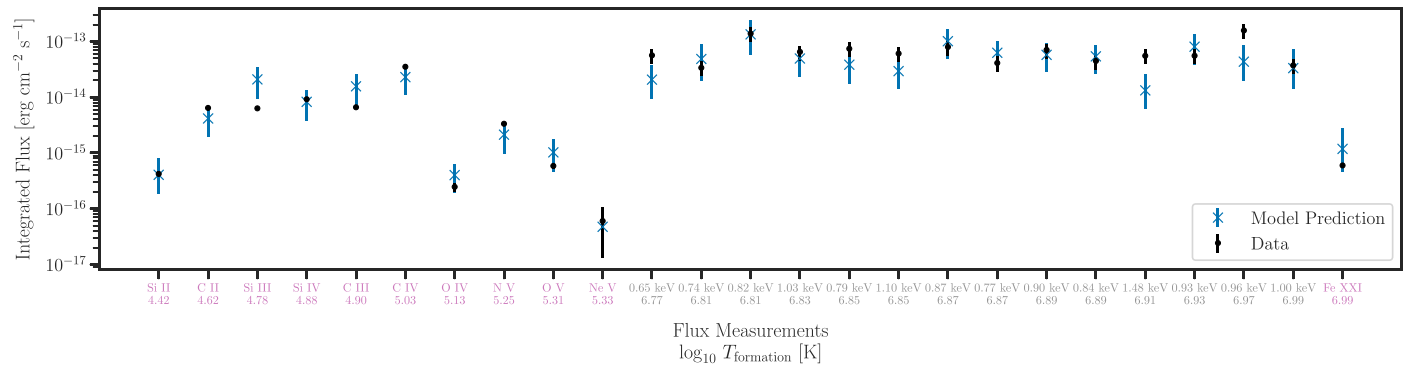


Figure 6. The observed flux constraints are plotted as black points with error bars corresponding to their measurement uncertainties while the DEM model predictions are plotted as light blue crosses with error bars corresponding to the 16th–84th percentile values of the distribution of fluxes predicted by drawing from the posterior of DEM shapes and the fractional flux systematic uncertainty parameter. The flux constraints are divided into two categories: ion species corresponding to integrated FUV emission line fluxes (labeled in pink) and central energies corresponding to the integrated flux of X-ray spectral bins (labeled in gray). Beneath each flux constraint’s label is its $\log_{10}(T_{\text{formation}} [\text{K}])$ value and the constraints are ordered by formation temperature increasing to the right.

fluxes from the DEM to the observed values and is a more direct visual representation of the model’s goodness of fit, while Table 4 compares the observations and model predictions for all flux constraints used in the DEM-fitting process. As the width of the uncertainty swath in Figure 5 indicates, the lack of observational constraints leads to high uncertainties at temperatures around 10^6 K, the regime where the majority of EUV flux is formed. Direct observations of stellar EUV emission are necessary to reduce this uncertainty for any modeling approach.

The FUV and X-ray data were not taken simultaneously and if there were unresolved flares in either data set the nonsimultaneity would introduce discrepancies between the predicted EUV emission and the true quiescent spectrum of V1298 Tau. However, the good agreement between both X-ray observations indicates that they were at similar levels of flare activity, while no significant flares were noted in the FUV photon event lightcurve. The DEM average for the FUV Fe XXI line also agrees well with the constraints from the X-ray data,

suggesting that any activity level discrepancies between these observations fall within the uncertainty of the measurements and fitting process.

4.2. EUV Spectrum

As mentioned above, we have improved the method of Duvvuri et al. (2021) to include recombination continua from hydrogen and helium species which adds bound-free edges, most notably the H I recombination edge short of 912 Å. In addition to propagating uncertainties with more specificity to all the observations of an individual star, an advantage of the DEM over scaling relations is the ability to synthesize an actual spectrum with higher wavelength resolution than the integrated flux across 100 Å bandpasses. While the DEM cannot predict line profiles, predicting the flux from individual optically thin emission lines allows spectral synthesis at a resolution where the width of a line is contained within a single spectral bin. This is especially important for modeling atmospheric escape from

Table 4
Integrated Fluxes of Optically thin FUV Emission Lines and X-ray Spectral Bins Compared to the DEM Predictions

Emission Feature	Wavelengths (Å)	$\log_{10} T_{\text{formation}}$ $\log_{10}(\text{[K]})$	Observed Flux ($10^{-15} \text{ erg s}^{-1} \text{ cm}^{-2}$)	DEM Prediction ($10^{-15} \text{ erg s}^{-1} \text{ cm}^{-2}$)
Si II	1260.4, 1264.7	4.42	0.51 ± 0.06	$0.40^{+0.38}_{-0.22}$
C II	1335 multiplet	4.62	6.42 ± 0.436	$4.2^{+2.7}_{-2.2}$
Si III	1294.5, 1301.1	4.78	6.53 ± 0.314	21^{+13}_{-11}
Si IV	1393.7, 1402.7	4.88	9.18 ± 0.751	$8.1^{+5.4}_{-4.2}$
C III	1175 multiplet	4.90	6.6 ± 0.314	$16^{+10}_{-8.5}$
C IV	1548.1, 1550.7	5.03	35.1 ± 3.02	23^{+14}_{-12}
O IV	1401.1	5.13	0.247 ± 0.044	$0.41^{+0.24}_{-0.21}$
N V	1238.8, 1242.8	5.25	3.34 ± 0.244	$2.1^{+1.3}_{-1.1}$
O V	1371.3	5.31	$0.587 \pm 0.05.84$	$1.0^{+0.76}_{-0.56}$
Ne V	1145.6	5.33	0.0604 ± 0.047	$0.047^{+0.040}_{-0.026}$
0.65 keV	19.1 ± 0.31	6.77	56 ± 17	21^{+16}_{-11}
0.74 keV	16.7 ± 0.27	6.81	34 ± 10	49^{+40}_{-28}
0.82 keV	15.2 ± 0.25	6.81	140 ± 41	130^{+100}_{-75}
1.03 keV	12.1 ± 0.20	6.83	65 ± 19	50^{+30}_{-26}
0.79 keV	15.7 ± 0.26	6.85	74 ± 22	38^{+25}_{-20}
1.10 keV	11.3 ± 0.19	6.85	61 ± 18	29^{+19}_{-15}
0.87 keV	14.2 ± 0.21	6.87	79 ± 24	100^{+60}_{-53}
0.77 keV	16.2 ± 0.27	6.87	41 ± 12	63^{+38}_{-33}
0.90 keV	13.7 ± 0.15	6.89	70 ± 21	58^{+34}_{-30}
0.84 keV	14.7 ± 0.24	6.89	45 ± 13	54^{+32}_{-27}
1.48 keV	8.40 ± 0.14	6.91	55 ± 17	$13^{+11}_{-7.0}$
0.93 keV	13.3 ± 0.22	6.93	55 ± 17	81^{+54}_{-42}
0.96 keV	12.9 ± 0.21	6.97	160 ± 47	43^{+43}_{-24}
1.00 keV	12.5 ± 0.20	6.99	37 ± 11	33^{+38}_{-19}
Fe XXI	1354.0	6.99	0.598 ± 0.0576	$1.2^{+1.67}_{-0.70}$

Note. In cases where multiple transitions are listed for the same ion, the reported flux is the summed flux across all listed transitions. For X-ray spectral bins, we list the central energy, wavelength, and wavelength bin width.

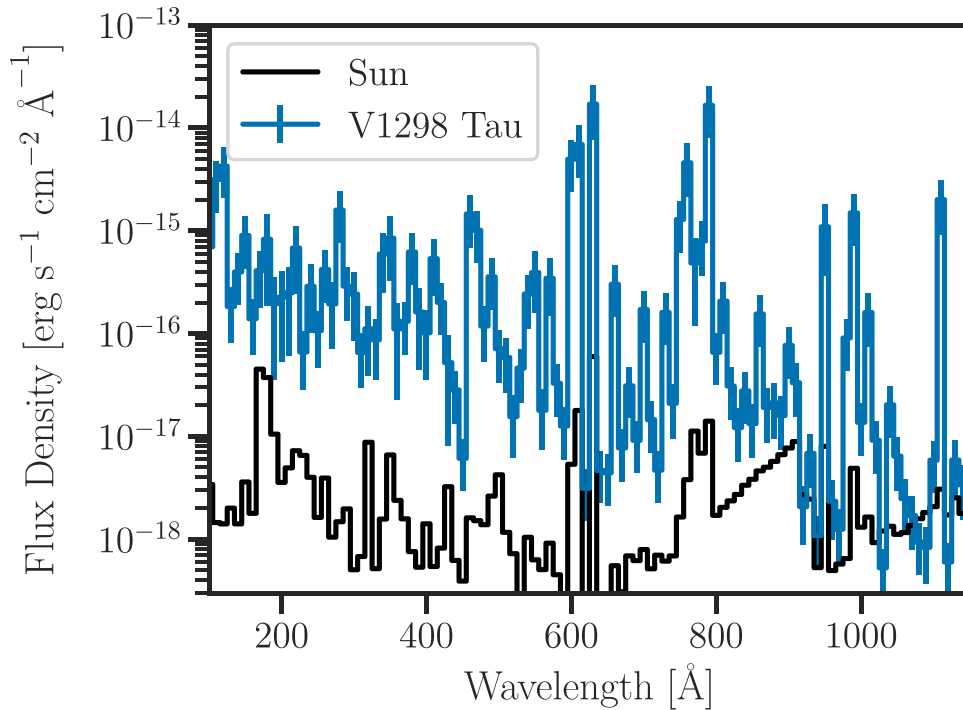


Figure 7. The EUV spectrum of V1298 Tau (light blue) compared to the EUV spectrum of the quiescent Sun (Woods et al. 2009). The EUV spectrum of younger, more active V1298 Tau is consistently a factor of 100–1000 greater than the Sun's across this wavelength regime, with a shallower slope for the H I continuum blueward of 912 Å forming the base of the strong emission lines.

Table 5
X-ray Fluxes Reported Across three Sets of Observations from Poppenhaeger et al. (2021), Maggio et al. (2023), and This Work

Reference	X-Ray Telescope	Observation Period	Best-fit Model Unabsorbed $F_{0.1-2.4 \text{ keV}}$ ($10^{-12} \text{ erg s}^{-1} \text{ cm}^{-2}$)
Poppenhaeger et al. (2021)	ROSAT + Chandra	1991 + November 2019	0.92 ± 0.1
This work	NICER	October/November 2020	1.74 ± 0.025
Maggio et al. (2023)	XMM-Newton	August 2021 (quiescent)	$1.4_{-0.2}^{+0.1}$
Maggio et al. (2023)	XMitNewton	August 2021 (elevated)	$1.82_{-0.08}^{+0.03}$

Note. The best-fit models indicate that the coronal flux of V1298 Tau has varied by a factor of 2 between 2019 and 2021 while the intra-observation variability has been $<30\%$.

Table 6
Broken Power Laws Describing the Evolution of Bandpass Fluxes for Solar-type Stars Determined by Linking the Ribas et al. (2005) Relations to the V1298 Tau SED Collated in this Work

Bandpass i [Å]	Flux at 1 au $F_{V1298\text{Tau},i}$ ($\text{erg s}^{-1} \text{ cm}^{-2}$)	α_i^a ($\text{erg s}^{-1} \text{ cm}^{-2}$)	β_i^a (-)	$t_{\text{crit},i}$ (Myr)
1–20	685	2.4	-1.92	53 ± 1
20–100	480	4.45	-1.27	25 ± 1
100–360	192	13.5	-1.2	110 ± 30
360–920 ^b	127	4.56	-1	36 ± 7

Notes.

^a Table 5 of Ribas et al. (2005).

^b No data for stars other than the Sun were available for this bandpass so Ribas et al. (2005) calibrated the power law by assuming $\beta = -1$ and solving for α to match the observed flux from the Sun.

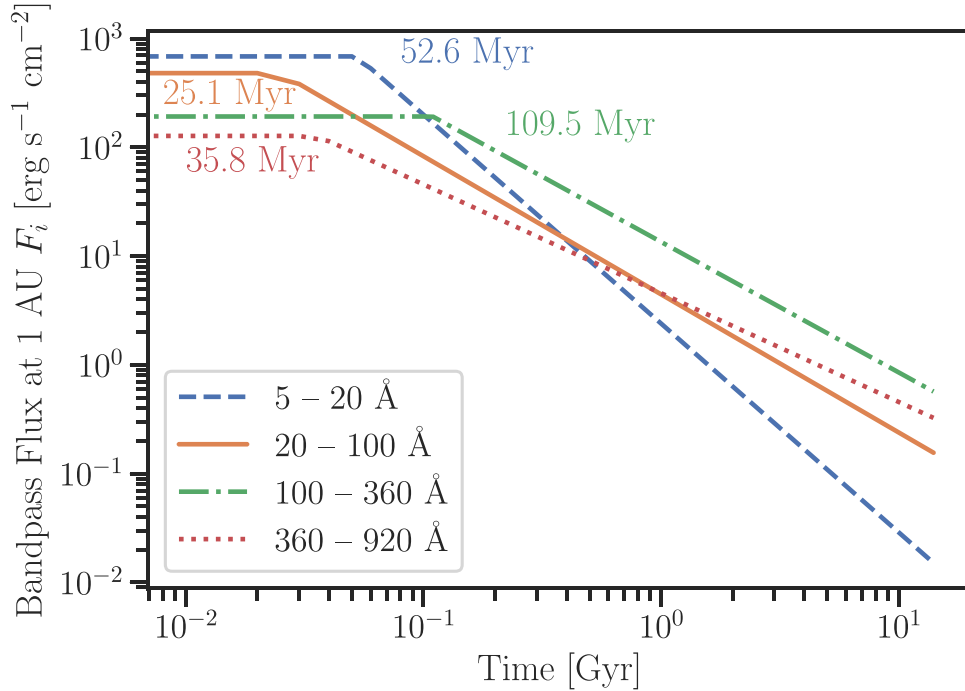


Figure 8. The broken-power laws describing the evolution of high-energy emission for solar-mass stars divided into 4 bandpasses, annotated with the time corresponding to the breakpoint of the power law: 1–20 Å (dashed dark blue; 52.9 Myr), 20–100 Å (solid orange, 24.2 Myr), 100–360 Å (dotted–dashed green, 108.7 Myr), 360–920 Å (dotted red; 35.9 Myr). The parameters for the broken-power laws are listed in Table 6.

the exospheres of irradiated exoplanets with methods more sophisticated than energy-limited escape. As observations of the He I 10830 Å line become increasingly accessible for exoplanets, Oklopčić (2019) demonstrates the necessity of well-characterized EUV and mid-UV spectra with uncertainties to interpret those observations.

One set of parameters from the posterior distribution describes the shape of the DEM and the intrinsic uncertainty on fluxes predicted by that DEM. For each sample draw from the posterior we calculate Ψ using the Chebyshev coefficients, predict the flux f in 1 Å bins from 1 to 2000 Å using the contribution functions of all lines that CHIANTI lists within the wavelength bin, and then sample from a Gaussian

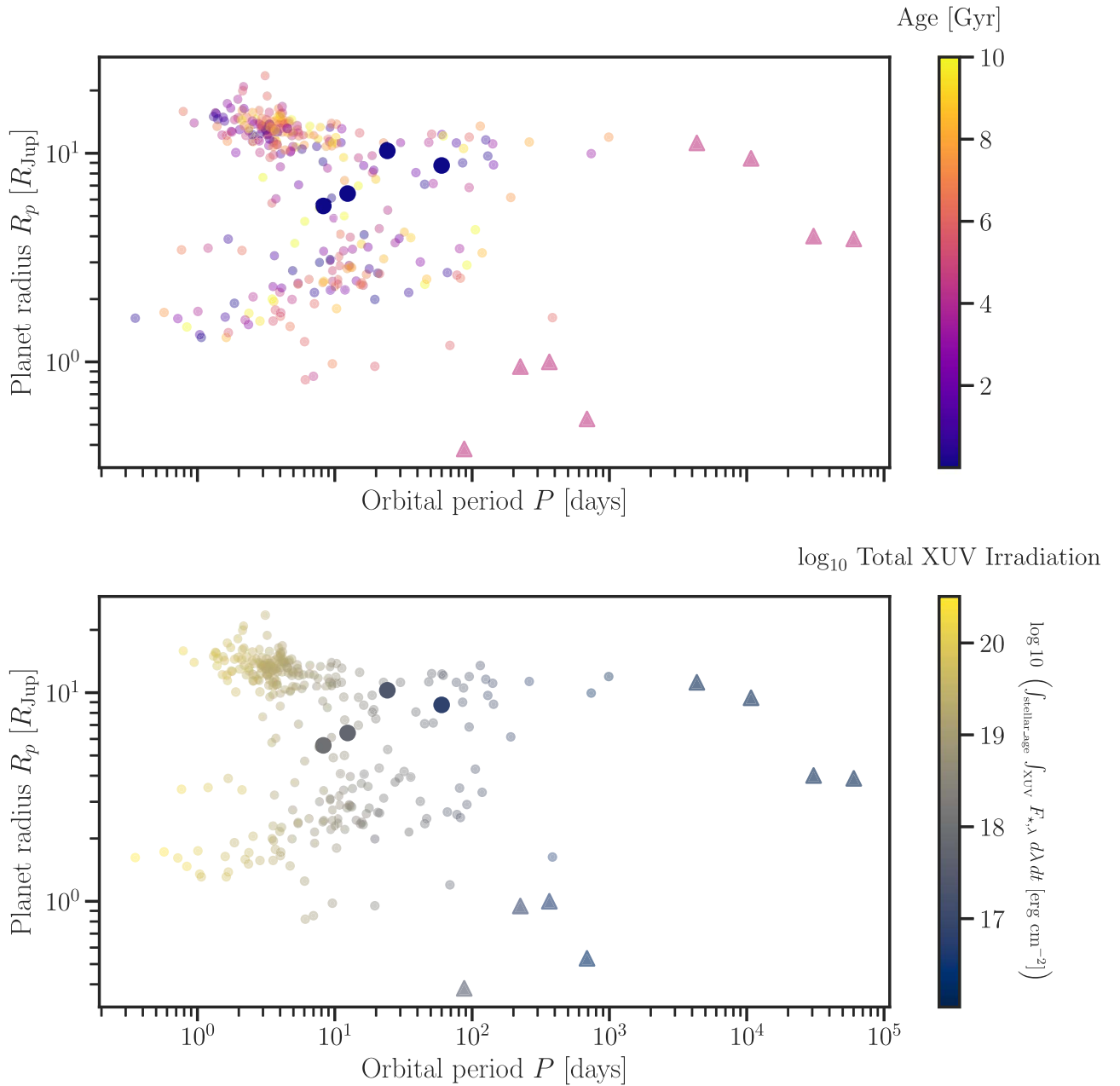


Figure 9. Both panels plot the planet radius against the orbital period for: a sample of confirmed exoplanets orbiting stars with a mass similar to V1298 Tau (translucent dots), the V1298 Tau planets (opaque circles), and solar system planets (opaque triangles). The top panel colors the planet markers by the age of the star, with darker shades representing young systems and increasing brightness with age, while the bottom panel colors the planet markers by the cumulative XUV irradiation experienced by the planet (F_* is the flux received by the planet) assuming it has stayed at its current orbit for the entirety of the system’s age, with the brightness of the color increasing with irradiation. For this sample selected by stellar mass, where all plotted planets are assumed to have experienced the same high-energy evolution, the cumulative XUV irradiation is a function of age. In a broader sample, where different stellar hosts follow different XUV irradiation evolution behavior, the cumulative XUV irradiation will also depend on other parameters like stellar mass.

$\mathcal{N}(\mu = f, \sigma = s \cdot f)$ where s is the fractional systematic uncertainty parameter. This creates one spectrum output corresponding to the single draw of parameters from the posterior distribution. After 10^6 such draws we record the 16th, 50th, and 84th percentile values of the flux in each wavelength bin to infer the EUV spectrum and the uncertainty of the inference. Figure 7 shows the EUV portion of the predicted spectrum compared to the Solar Irradiance Reference Spectrum from Woods et al. (2009) scaled to the distance from V1298 Tau, illustrating how youth and activity enhance the flux of V1298 Tau across the entire EUV regime. The integrated XUV (X-ray + EUV, $<912 \text{ \AA}$) flux from V1298 Tau using our

combination of the XSPEC model and the DEM-generated EUV spectra is $3.2 \pm 0.3 \times 10^{-12} \text{ erg s}^{-1} \text{ cm}^{-2}$ with additional uncertainty scaling factors of 15% and 20% introduced to the SED for the FUV flux calibration and $n(\text{H I})$ column density uncertainties, respectively.

Poppenhaeger et al. (2021) and more recently Maggio et al. (2023) have also estimated the total EUV flux of V1298 Tau using different sets of observations and methods than this work. Between all three sets of observations, it is clear in the data that V1298 Tau exhibits significant long-term X-ray variability, but assessing the EUV variability is more difficult given the model-dependence of the EUV estimation. The X-ray fluxes reported

by Poppenhaeger et al. (2021), Maggio et al. (2023), and this work are listed in Table 5.

Maggio et al. (2023) fits emission measure distributions to two sets of observations with different X-ray fluxes labeled “quiescent” and “elevated,” finding that the bulk of the difference in X-ray flux can be attributed to the enhancement of a hotter 10^7 K plasma component in the elevated state. This would likely have a small impact on the EUV variability since the majority of EUV flux is formed between $10^{5.5}$ and $10^{6.5}$ (Duvvuri et al. 2021). If there is significant EUV variability in this system, either between or during observations, it will affect both the detection of atmospheric escape and the inference of mass-loss rates via transmission spectroscopy, and this possibility should be considered in future analyses of planets in this system.

5. Conclusion

As the star spins down, the nonthermal heating of the star’s upper atmosphere will decrease over time and reduce the high-energy emission from V1298 Tau, but not necessarily by a constant value across the XUV wavelength regime depending on how the evolution varies at different stellar atmospheric heights and temperatures (Ribas et al. 2005). The long-term fate of V1298 Tau’s planets will depend on how the photoevaporative mass-loss changes over the lifetime of the system. Ribas et al. (2005) assembled spectra of seven solar-mass stars (0.9 – $1.1 M_{\odot}$) across a wide range of ages, including EUVE data, to characterize these stars’ evolution of high-energy emission over time. Ribas et al. (2005) fit power laws to the integrated flux for 3 XUV bandpasses: 1–20, 20–100, and 100–360 Å and assigned a power law for the 360–920 Å bandpass. More recent work like Wright et al. (2011) has favored a broken-power law for X-ray emission, observing that for the youngest stars, the X-ray emission clusters around a saturation value, well below what the Ribas et al. (2005) power laws would predict if allowed to extend to those young ages.

V1298 Tau is not a perfect Young Sun analog, but the original planet discovery paper, David et al. (2019b), estimated that V1298 Tau would settle close to either side of the F/G cusp. Tables 5 and 6 from Pecaut & Mamajek (2013)⁷ predict that a star of this mass will settle on the main sequence as a $T_{\text{eff}} = 6000$ K F9–F9.5V star, and V1298 Tau is old enough that its mass should not change significantly during that process. This would make the future main-sequence V1298 Tau very similar to β Comae Berenices, the hottest star in the Ribas et al. (2005) sample (G0V, $T_{\text{eff}} = 6000$ K, $M_{\star} = 1.1 M_{\odot}$), used to anchor the power-law relations at 1.6 Gyr. By taking V1298 Tau to be representative of the saturation flux for young solar-mass stars, we modify the Ribas et al. (2005) power laws to be broken-power laws that follow

$$F_i = \begin{cases} F_{V1298\text{Tau},i} & \text{if } t < t_{\text{crit},i} \\ \alpha_i \left(\frac{t}{1\text{Gyr}} \right)^{\beta_i} & \text{if } t \geq t_{\text{crit},i} \end{cases} \quad (1)$$

where i represents the individual bandpass intervals, $F_{V1298\text{Tau},i}$ is the flux of V1298 Tau scaled to a distance of 1 au and integrated over the bandpass i , α_i and β_i are taken from Table 5 of Ribas et al. (2005), and we solve for the breakpoint of the

power law $t_{\text{crit},i} = \sqrt[\beta_i]{\frac{F_{V1298\text{Tau},i}}{\alpha_i}}$ by requiring the function to be continuous. The parameters for this broken-power law are listed in Table 6 and the functions are plotted in Figure 8. The reported uncertainties on t_{crit} only incorporate the uncertainty of the V1298 Tau SED and are therefore underestimates: the Ribas et al. (2005) power laws were calibrated with only one solar analog at each representative age of their sample, and the 360–920 Å bandpass was only anchored by the Sun and an assumed power-law slope. Determining the true evolution of this EUV bandpass is important for characterizing atmospheric escape and the relationship between spin down and weakening stellar magnetism. Ribas et al. (2005) notes that the power-law slopes grow shallower with increasing bandpass wavelengths, a trend in agreement with the finding from Ayres (1999) that the emission from hotter plasma decays more rapidly. A related observation from Pineda et al. (2021) is that the t_{crit} values for broken-power laws fit to rotation-age-activity relations from FUV emission lines (transition region) are later than those derived from X-ray emission (corona). This work’s broken-power law for the 360–920 Å bandpass diverges significantly from these findings in the literature, but is also the least constrained by data. Observations of the multiwavelength behavior of both the decay slope and breakpoint from activity saturation would be powerful tests for physical models of stellar magnetic evolution.

The combination of transit surveys and Gaia has made it possible to identify exoplanet systems in moving groups and associations with known ages, increasing the number of systems with precisely known ages. We queried the Exoplanet Archive⁸ for all confirmed exoplanets with known radii and orbital periods orbiting stars with $0.9 < M_{\star} < 1.2 M_{\odot}$ (similar to V1298 Tau $M_{\star} = 1.1 M_{\odot}$) and a reported age with an uncertainty less than a factor of 2, then applied the broken-power-law evolution to each planetary system to determine the cumulative XUV irradiation of each planet (flux received by the planet integrated over XUV wavelengths and the lifetime of the system), plotted in Figure 9. The planets of the V1298 Tau system are in a relatively sparse region of the plot, but there are a wide range of ages and XUV irradiation values represented among these planets’ closest neighbors, with fairly little variation of total irradiation across planets near a particular orbital period. This is because of the rapid decay of XUV emission past 0.1 Gyr for solar-mass stars, leading to little difference in the cumulative irradiation for all but the youngest exoplanets orbiting this spectral type. However, the relatively later and slower decay of XUV emission from cooler exoplanet hosts (Linsky et al. 2020) will complicate the dominance of orbital period in a more mixed sample of exoplanets. Looking for trends in XUV irradiation and planet demographics will require filling out this plot and others like it with different planetary parameters by increasing the range of stellar types with well-characterized XUV evolution.

As exoplanet surveys continue to detect viable systems for atmospheric characterization via transmission spectroscopy and direct-imaging, interpreting these observations and studying atmospheric evolution requires more detailed stellar characterization beyond spectral type. V1298 Tau is one of the brightest exoplanet hosts accessible within our solar neighborhood

⁷ updated version hosted at: https://www.pas.rochester.edu/~emamajek/EEM_dwarf_UBVIJHK_colors_Teff.txt.

⁸ <https://exoplanetarchive.ipac.caltech.edu/>

($d = 108.5$ pc) and we still require model-dependent estimates of its high-energy emission. This star is an unusual case where the EUV uncertainties are more tightly constrained than the Ly α recovery, but both wavelength regimes need next-generation observatories to improve our understanding of stellar magnetism and the evolution of exoplanet atmospheres. This paper presents a roadmap for calculating empirically informed spectra of exoplanet host stars that can be used until those observatories become available.

Acknowledgments

We thank the anonymous referee for the comments that clarified and improved the discussion of this work. This research has made use of data and software provided by the High Energy Astrophysics Science Archive Research Center (HEASARC), which is a service of the Astrophysics Science Division at NASA/GSFC, made use of software provided by the Chandra X-ray Center (CXC) in the application packages CIAO and Sherpa, and made use of the NASA Exoplanet Archive, which is operated by the California Institute of Technology, under contract with the National Aeronautics and Space Administration under the Exoplanet Exploration Program. This work used atomic data from CHIANTI, a collaborative project involving George Mason University, the University of Michigan (USA), University of Cambridge (UK) and NASA Goddard Space Flight Center (USA). This work is partially based upon effort supported by NASA under award 80NSSC22K0076 and was supported by grant HST-GO-16163 to the University of Colorado. All the HST data used in this paper can be found in MAST:[10.17909/v5c1-4563](https://archive.stsci.edu/mast/10.17909/v5c1-4563).

Facilities: HST: STIS (Woodgate et al. 1998), HST: COS (Green et al. 2012), NICER (Gendreau et al. 2016).

Software: Astropy (Astropy Collaboration et al. 2013, 2018, 2022), bibmanager (Cubillos 2020), CHIANTI (Dere et al. 1997; Del Zanna et al. 2021), CIAO (Freeman et al. 2001), HEASoft (Nasa High Energy Astrophysics Science Archive Research Center (Heasarc), 2014), emcee (Foreman-Mackey et al. 2013), matplotlib (Hunter 2007), numpy (Harris et al. 2020), pandas (pandas development team 2020; Wes McKinney 2010; pandas development team 2020), seaborn (Waskom 2021), XSPEC (Arnaud 1996).

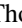
ORCID iDs

Girish M. Duvvuri  <https://orcid.org/0000-0002-7119-2543>

P. Wilson Cauley  <https://orcid.org/0000-0001-9207-0564>

Fernando Cruz Aguirre  <https://orcid.org/0000-0003-4628-8524>

Kevin France  <https://orcid.org/0000-0002-1002-3674>

Zachory K. Berta-Thompson  <https://orcid.org/0000-0002-3321-4924>

J. Sebastian Pineda  <https://orcid.org/0000-0002-4489-0135>

References

- Arnaud, K. A. 1996, in ASP Conf. Ser. 101, *Astronomical Data Analysis Software and Systems V*, ed. G. H. Jacoby & J. Barnes (San Francisco, CA: ASP), 17
- Ayres, T. R. 1999, *ApJ*, **525**, 240
- Astropy Collaboration, Price-Whelan, A. M., Lim, P. L., et al. 2022, *ApJ*, **935**, 167
- Astropy Collaboration, Price-Whelan, A. M., Sipőcz, B. M., et al. 2018, *AJ*, **156**, 123
- Astropy Collaboration, Robitaille, T. P., Tollerud, E. J., et al. 2013, *A&A*, **558**, A33
- Craig, I. J. D., & Brown, J. C. 1976, *A&A*, **49**, 239
- Cruz Aguirre, F., Youngblood, A., France, K., & Bourrier, V. 2023, *ApJ*, **946**, 98
- Cubillos, P. E. 2020, bibmanager: A BibTeX manager for LaTeX projects, Zenodo, doi:[10.5281/zenodo.2547042](https://doi.org/10.5281/zenodo.2547042)
- David, T. J., Petigura, E. A., Luger, R., et al. 2019a, *ApJL*, **885**, L12
- David, T. J., Cody, A. M., Hedges, C. L., et al. 2019b, *AJ*, **158**, 79
- Del Zanna, G., Dere, K. P., Young, P. R., & Landi, E. 2021, *ApJ*, **909**, 38
- Dere, K. P., Landi, E., Mason, H. E., Monsignori Fossi, B. C., & Young, P. R. 1997, *A&AS*, **125**, 149
- Diamond-Lowe, H., Kreidberg, L., Harman, C. E., et al. 2022, *AJ*, **164**, 172
- Diamond-Lowe, H., Youngblood, A., Charbonneau, D., et al. 2021, *AJ*, **162**, 10
- Duvvuri, G. M., Pineda, J. S., Berta-Thompson, Z. K., et al. 2021, *ApJ*, **913**, 40
- Feinstein, A. D., France, K., Youngblood, A., et al. 2022, *AJ*, **164**, 110
- Feinstein, A. D., Montet, B. T., Johnson, M. C., et al. 2021, *AJ*, **162**, 213
- Fontenla, J. M., Linsky, J. L., Witbrod, J., et al. 2016, *ApJ*, **830**, 154
- Foreman-Mackey, D., Hogg, D. W., Lang, D., & Goodman, J. 2013, *PASP*, **125**, 306
- France, K., Duvvuri, G., Egan, H., et al. 2020, *AJ*, **160**, 237
- France, K., Loyd, R. O. P., Youngblood, A., et al. 2016, *ApJ*, **820**, 89
- France, K., Schindhelm, R., Herczeg, G. J., et al. 2012, *ApJ*, **756**, 171
- Freeman, P., Doe, S., & Siemiginowska, A. 2001, *Proc. SPIE*, **4477**, 76
- Fulton, B. J., Petigura, E. A., Howard, A. W., et al. 2017, *AJ*, **154**, 109
- Gendreau, K. C., Arzoumanian, Z., Adkins, P. W., et al. 2016, *Proc. SPIE*, **9905**, 99051H
- Ginzburg, S., Schlichting, H. E., & Sari, R. 2018, *MNRAS*, **476**, 759
- Goodman, J., & Weare, J. 2010, *CAMCS*, **5**, 65
- Green, J. C., Froning, C. S., Osterman, S., et al. 2012, *ApJ*, **744**, 60
- Gaia Collaboration, Brown, A. G. A., Vallenari, A., et al. 2018, *A&A*, **616**, A1
- Harris, C. R., Millman, K. J., van der Walt, S. J., et al. 2020, *Natur*, **585**, 357
- Hunter, J. D. 2007, *CSE*, **9**, 90
- Husser, T. O., Wende-von Berg, S., Dreizler, S., et al. 2013, *A&A*, **553**, A6
- Kashyap, V., & Drake, J. J. 1998, *ApJ*, **503**, 450
- King, G. W., & Wheatley, P. J. 2021, *MNRAS*, **501**, L28
- Linsky, J. L., Fontenla, J., & France, K. 2014, *ApJ*, **780**, 61
- Linsky, J. L., Wood, B. E., Youngblood, A., et al. 2020, *ApJ*, **902**, 3
- Louden, T., Wheatley, P. J., & Briggs, K. 2017, *MNRAS*, **464**, 2396
- Maggio, A., Pillitteri, I., Argiroffi, C., et al. 2023, *ApJ*, **951**, 18
- Markwardt, C. B. 2009, in ASP Conf. Ser. 411, *Astronomical Data Analysis Software and Systems XVIII*, ed. D. A. Bohlender, D. Durand, & P. Dowler (San Francisco, CA: ASP), 251
- Nasa High Energy Astrophysics Science Archive Research Center (Heasarc) 2014, HEASoft: Unified Release of FTOOLS and XANADU, Astrophysics Source Code Library, ascl:[1408.004](https://www.ascl.net/1408.004)
- Oklopčić, A. 2019, *ApJ*, **881**, 133
- pandas development team, T 2020, pandas-dev/pandas: Pandas, v2.0.3, Zenodo, doi:[10.5281/zenodo.3509134](https://doi.org/10.5281/zenodo.3509134)
- Peacock, S., Barman, T., Shkolnik, E. L., et al. 2020, *ApJ*, **895**, 5
- Pecaut, M. J., & Mamajek, E. E. 2013, *ApJS*, **208**, 9
- Pineda, J. S., Youngblood, A., & France, K. 2021, *ApJ*, **911**, 111
- Poppenhaeger, K., Ketzer, L., & Mallonn, M. 2021, *MNRAS*, **500**, 4560
- Raymond, J. C., & Smith, B. W. 1977, *ApJS*, **35**, 419
- Remillard, R. A., Loewenstein, M., Steiner, J. F., et al. 2022, *AJ*, **163**, 130
- Ribas, I., Guinan, E. F., Güdel, M., & Audard, M. 2005, *ApJ*, **622**, 680
- Rogers, J. G., Gupta, A., Owen, J. E., & Schlichting, H. E. 2021, *MNRAS*, **508**, 5886
- Sanz-Forcada, J., Favata, F., & Micela, G. 2004, *A&A*, **416**, 281
- Sanz-Forcada, J., Micela, G., Ribas, I., et al. 2011, *A&A*, **532**, A6
- Tilipman, D., Vieytes, M., Linsky, J. L., Buccino, A. P., & France, K. 2021, *ApJ*, **909**, 61
- Waskom, M. L. 2021, *JOSS*, **6**, 3021
- Watson, A. J., Donahue, T. M., & Walker, J. C. G. 1981, *Icar*, **48**, 150
- Wes McKinney 2010, in *Python in Science Conf.* Vol. 445ed. S. van der Walt & J. Millman (Austin, TX: SciPy), 56
- Wood, B. E., Redfield, S., Linsky, J. L., Müller, H.-R., & Zank, G. P. 2005, *ApJS*, **159**, 118
- Woodgate, B. E., Kimble, R. A., Bowers, C. W., et al. 1998, *PASP*, **110**, 1183
- Woods, T. N., Chamberlin, P. C., Harder, J. W., et al. 2009, *GeoRL*, **36**, L01101
- Wright, N. J., Drake, J. J., Mamajek, E. E., & Henry, G. W. 2011, *ApJ*, **743**, 48
- Youngblood, A., France, K., Loyd, R. O. P., et al. 2016, *ApJ*, **824**, 101